Wind-Induced Buffeting Vibration of Long-Span Bridge Considering Geometric and Aerodynamic Nonlinearity Based on Reduced-Order Modeling

Wei Cui, A.M.ASCE[1]; Lin Zhao[2]; and Yaojun Ge[3]

Abstract: Aeroelastic instability and buffeting are two wind-induced phenomena for long-span bridges. In the traditional method, aeroelastic instability and buffeting are analyzed separately. If geometric and aerodynamic nonlinearity are required, aeroelastic instability is normally calculated based on finite-element methods, and buffeting is carried out based on linearization of structural and aerodynamic nonlinearity. Then, the standard frequency-domain methods are utilized on the eigenvalue decomposition. However, for ultralong-span bridges, aerostatic deformation, aeroelasticity, and buffeting are strongly coupled. During buffeting, the bridge deck pitching will change both structural stiffness and aerodynamic loads; therefore, the nonlinearity should be included in the long-span bridge buffeting analysis. This paper establishes a reduced-order modeling procedure to simulate the wind-induced buffeting vibration for long-span bridges including the nonlinear aeroelasticity and buffeting force. First, the mode-based vibration formulas are derived to consider both structural and aerodynamic nonlinearity through polynomial expansion. Next, the numerically simulated turbulence is imported into the vibration governing equation, and the structural response can be calculated using the time-domain integration method. **DOI: 10.1061/JSENDH.STENG-11543.** © *2023 American Society of Civil Engineers.*

Author keywords: Long-span bridge; Wind-induced buffeting vibration; Structural nonlinearity; Aerodynamic nonlinearity; Reduced-order modeling.

Introduction

Suspension bridges can achieve a longer main span than any other type of bridge structure and are widely used all over the world to cross natural obstacles, such as seawater and canyons. The main span of a suspension bridges has kept growing in the last century and continued to grow in this century. The Golden Gate Bridge built in 1937 has a main span of 1,280 m, the span of the Great Belt Bridge constructed in 1998 is 1,624 m, the Akashi Kaikyō Bridge is 1,991 m currently, and the Çanakkale 1915 Bridge, with a 2,023-m main span, is the current longest bridge. However, several bridges under construction have main spans longer than 2,000 m, such as Zhanggao Bridge with a main span of 2,300 m. The long-planned Messina Bridge bridge has a main span of 3,300 m.

As the span of bridges continues to grow, their structural stiffness rapidly reduces and their mass increases correspondingly. As a result, the long-span bridge is vulnerable to wind effects. Traditionally, researchers focused on the two types of wind-induced instability: flutter and torsional divergence (Xiang and Ge 2002). Flutter is caused by the increasing periodic motion of a bridge section, for example, the collapse of the Tacoma Narrow Bridge (Amman et al. 1941), and torsional divergence happens when the static wind load is greater than the structural resistance.

At first, geometry nonlinearity and aerodynamic nonlinearity were included in the torsional divergence analysis for long-span bridges. Next, the nonlinear aeroelastic effects for the postflutter region have been investigated by various researchers, and many different aerodynamic force models were developed (Gao et al. 2018; Zhang et al. 2021, 2019; Li et al. 2021). The nonlinear aeroelastic force was also investigated in wind tunnels through free vibration (Gao et al. 2020) and forced vibration (Liu et al. 2022).

The two aforementioned aerodynamic phenomena occur only considering laminar wind flow. However, the turbulence is a non-negligible part of the atmospheric boundary layer, especially in tropical cyclones (Zhao et al. 2019; Cao et al. 2009; Wang et al. 2016) and tornadoes (Wang et al. 2017). Correspondingly, turbulence-induced random vibration, also known as buffeting, is an important part of the structural response in strong winds (Cui and Caracoglia 2018b). Regularly, buffeting is analyzed according to the famous Davenport wind loading chain (Davenport 1962) in the frequency domain. The frequency-domain analysis requires the wind–bridge interaction dynamic system to be linear for both structural part and aerodynamic part (Cui and Caracoglia 2018a). On the other hand, time-domain simulation based on a rational function was developed to use an iterative procedure to simulate nonlinear aerodynamic effects (Chen et al. 2000).

[1]Assistant Professor, State Key Lab of Disaster Reduction in Civil Engineering, Tongji Univ., Shanghai 200092, China; Key Laboratory of Transport Industry of Wind Resistant Technology for Bridge Structures, Tongji Univ., Shanghai 200092, China; Dept. of Bridge Engineering, College of Civil Engineering, Tongji Univ., Shanghai 200092, China. ORCID: https://orcid.org/0000-0001-7489-923X. Email: cuiwei@tongji.edu.cn

[2]Professor, State Key Lab of Disaster Reduction in Civil Engineering, Tongji Univ., Shanghai 200092, China; Professor, Key Laboratory of Transport Industry of Wind Resistant Technology for Bridge Structures, Tongji Univ., Shanghai 200092, China; Professor, Dept. of Bridge Engineering, College of Civil Engineering, Tongji Univ., Shanghai 200092, China (corresponding author). Email: zhaolin@tongji.edu.cn

[3]Professor, State Key Lab of Disaster Reduction in Civil Engineering, Tongji Univ., Shanghai 200092, China; Professor, Key Laboratory of Transport Industry of Wind Resistant Technology for Bridge Structures, Tongji Univ., Shanghai 200092, China; Professor, Dept. of Bridge Engineering, College of Civil Engineering, Tongji Univ., Shanghai 200092, China. Email: yaojunge@tongji.edu.cn

When a long-span bridge is affected by strong winds, strong nonlinearity occurs on both structural dynamics (geometry nonlinearity) and aerodynamic [large instantaneous angle of attack (Diana et al. 2010)]. Especially when the wind speed is close to the instability critical point, strong winds cause a large static torsional displacement, which changes the effective angle of attack and causes early aerodynamic instability. However, the traditional methods based on FEM cannot calculate the wind-induced structural vibration response with strong nonlinearity (Zhao et al. 2023) because the time steps required by strong nonlinear behavior become so small that the FEM simulation is extreme inefficient. Therefore, an analytical method is required to compute the structural nonlinear response under wind effects.

The nonlinear parametric modeling of suspension bridges was developed to study the aeroelastic effect on torsional divergence and flutter (Arena and Lacarbonara 2012), as well as the postcritical behavior of suspension bridge (Vickery et al. 2009). However, bridge vibration under turbulence considering structural and aerodynamic nonlinearity has been seldom investigated. Most previous studies about nonlinear buffeting were based on finite-element methods, which are difficult to converge when the wind speed is close to the critical points.

In order the efficiently simulate the nonlinear aeroelastic force, the quasi-steady method of bridge aeroelasticity was developed by Borri and Costa (2004). The fundamental theory of the quasi-steady method is implementation of both aeroelastic and buffeting forces (Costa et al. 2007) through the effective angle of attack. Because the aerodynamic coefficients vary nonlinearly with the angle of attack, the aeroelastic and buffeting forces will enter a nonlinear stage for large vibration amplitudes. Many widely used nonlinear aerodynamic models are based on the quasi-steady theory, such as those of Liu et al. (2022) and Wu et al. (2020). Therefore, the quasi-steady method provides an united framework to evaluate the nonlinear aeroelasticity and buffeting force for bridge decks. However, the unsteady effect cannot be fully included in the quasi-steady method, and the calculation of aeroelastic loads may be inaccurate for flow separation after a bluff body for a low wind speed.

On the other hand, the modeling of structural nonlinearity is also challenging because the large number of degrees of freedom. Therefore, a large number of reduced-order modeling methods have been developed to balance to the accuracy and computation efficiency. A detailed literature review about reduced-order modeling of nonlinear structures has been provided by Mignolet et al. (2013). The general philosophy of reduced-order modeling is projection of the structural load-displacement relationship from conventional coordinates onto generalized modal coordinates. Next, only a small number of generalized modes with more importance are selected and other modes are neglected to reduced the analyzed degrees of freedom number. The determination of reduced-order modeling includes the direct method (Przekop et al. 2004), displacement-based indirect method (Muravyov and Rizzi 2003), and force-based indirect methods (Hollkamp et al. 2005).

This paper provides an analytical method to calculate the strong wind-induced random vibration considering the structural and aerodynamic nonlinearity based on reduced-order modeling. This reduced-order framework to analyze the nonlinear wind-induced motion includes three aspects: nonlinear structural stiffness, nonlinear aerostatic force induced by averaged motion, and nonlinear aeroelastic force induced by vibration. The structure of this paper is as follows: first, the motion governing equation of the long-span bridge is decomposed into several selected dynamic modes as the reduced-order model. Next, the nonlinear structure stiffness and aerodynamics are approximated by polynomials of structural responses. The nonlinear structure is reduced to selected modes based

on deformation-based indirect methods. At last, the structural wind-induced vibration with and without turbulence can be simulated in the time domain based on the approximate reduced-order model. At large wind speed, the bridge structure exhibits many nonlinear dynamic phenomena, such as limit-cycle oscillation and beating vibration.

Mathematical Modeling of Long-Span Bridge Aeroelastic Instability

Formulation of Bridge Buffeting with Nonlinear Structural Stiffness and Aerodynamics

The wind loads per unit span applied on the bridge section can be decomposed into three components along the wind axis: drag force F_D, lift force F_L, and pitch moment F_M, which are caused by wind speed U with an initial angle of attack (AoA) α_0. The bridge motion is also decomposed into motion axis with three components: sway $p(x)$, hover $p(x)$, and pitch $\theta(x)$. The two axes systems are illustrated in Fig. 1.

The nonlinear equilibrium equations under static wind loads is

$$\boldsymbol{M}\ddot{\boldsymbol{d}} + \boldsymbol{C}\dot{\boldsymbol{d}} + \boldsymbol{K}(\boldsymbol{d}) = \boldsymbol{F}_s(U, \boldsymbol{d}) + \boldsymbol{F}_b(U, \boldsymbol{d}) \tag{1}$$

where $\boldsymbol{d}$ = three-dimensional bridge deck deflection along span co-ordinate x including three components: sway $p(x)$, hover $h(x)$, and pitch θ, and thus $\boldsymbol{d} = [\, p(x) \quad h(x) \quad \theta(x) \,]^T$; $\boldsymbol{K}(\boldsymbol{d})$ = nonlinear stiffness matrix depending on $\boldsymbol{d}$; and $\boldsymbol{F}(U, \boldsymbol{d})$ = static nonlinear wind load matrix depending on wind speeds U and $\boldsymbol{d}$ as well.

The unsteady aeroelastic force is ignored in this study because currently, there is no well-established and ready-to-use three-dimensional unsteady aeroelastic force model with large AoA. On the other hand, the purpose of this study is to investigate the interaction between buffeting and aerostatic deformation; therefore, the down-wash effect (vertical motion velocity) on angle of attack (Barni et al. 2021) is neglected in this study. Nevertheless, if the unsteady time-domain force model is ready, it can be plugged into the formula presented in this study directly.

The three-dimensional wind load vector along the bridge span can be expanded as follows:

$$\boldsymbol{F}_s(U, \boldsymbol{d}) = \frac{1}{2}\rho U^2 \begin{bmatrix} B & & \\ & B & \\ & & B^2 \end{bmatrix} \begin{bmatrix} C_D(\alpha_0 + \alpha) \\ C_L(\alpha_0 + \alpha) \\ C_M(\alpha_0 + \alpha) \end{bmatrix} \tag{2}$$

where ρ = air density; B = bridge deck width; α_0 = initial wind AoA; and C_D, C_L, and C_M = drag, lift, and pitch moment coefficients, respectively. C_D, C_L, and C_M are depending on the wind AoA α, whereas the effective AoA α is the summation of initial AoA α_0 and bridge girder motion-induced instantaneous AoA.
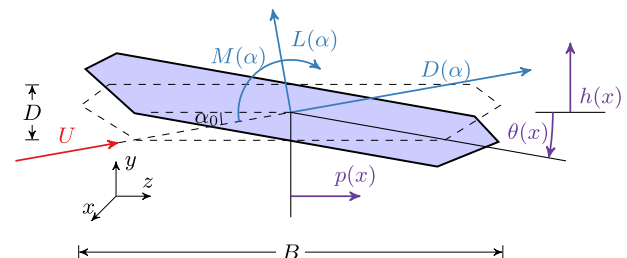

Fig. 1. Wind loads axis and bridge motion axis on bridge section.

According to quasi-steady theory of Borri and Costa (2004), the motion-induced instantaneous AoA is expressed

$$\alpha = \theta + \arctan\left(\frac{\dot{h} - 0.5B\dot{\theta}}{U}\right) \approx \theta + \frac{\dot{h} - 0.5B\dot{\theta}}{U} \quad (3)$$

Thus, the total wind static loads are nonlinear respect to bridge deck defection d.

The buffeting force is

$$F_b(U, d) = \frac{1}{2}\rho U^2 \begin{bmatrix} B & & \\ & B & \\ & & B^2 \end{bmatrix}$$

$$\times \begin{bmatrix} 2C_D(\alpha_0 + \alpha) & C_L(\alpha_0 + \alpha) + C_{D'}(\alpha_0 + \alpha) \\ 2C_L(\alpha_0 + \alpha) & C_D(\alpha_0 + \alpha) + C_{L'}(\alpha_0 + \alpha) \\ 2C_M(\alpha_0 + \alpha) & C_{M'}(\alpha_0 + \alpha) \end{bmatrix}$$

$$\times \begin{bmatrix} \dfrac{u(x,t)}{U}\chi_u(n) \\ \dfrac{w(x,t)}{U}\chi_w(n) \end{bmatrix} \quad (4)$$

where $C_{D'}$, $C_{L'}$, and C_M = derivatives of C_D, C_L, and C_M with respect to α; u and w = along-wind and vertical turbulence components, respectively; and $\chi_u(n)$ and $\chi_w(n)$ = aerodynamic admittance function for u and w.

The linear part of structural dynamics can be decomposed into modal coordinates as follows:

$$\hat{M}\ddot{q} + \hat{C}\dot{q} + \hat{K}_e q + \hat{K}_n(q) = \hat{F}_s + \hat{F}_b \quad (5)$$

where $\hat{M} = \Phi^T M \Phi$, $\hat{C} = \Phi^T C \Phi$ and $\hat{K} = \Phi^T K \Phi$ are modal generalized mass, damping, and stiffness; $\hat{K}_e = \Phi^T K_e \Phi$ and $\hat{K}_n(q) = \Phi^T K_n(d)\Phi$ are the linear part and nonlinear part of the modal generalized structural stiffness matrix; $\hat{F}_s = \Phi^T F_s$ and $\hat{F}_b = \Phi^T F_b$ = generalized aerostatic force and buffeting force respectively; Φ is the mode shape matrix; and Φ and $\hat{K}_e$ are generalized eigenvectors and eigenvalues of linear stiffness matrix K_e with respect to mass matrix M. For the bridge buffeting response induced by wind turbulence, normally only few modes are excited, therefore only Eq. (5) can be reduced to selected modes as a standard reduced-order modeling technique.

Polynomial Approximation of Nonlinear Aerodynamic Force

Taking the drag coefficient C_D as an example, the C_D varying with attack angle can be approximated by polynomials $\mathcal{P}_D^n(\alpha_0 + \alpha)$ to n degree

$$C_D(\alpha_0 + \alpha) \approx \mathcal{P}_D^n(\alpha_0 + \alpha)$$
$$= p_D^{(0)} + p_D^{(1)}\alpha + p_D^{(2)}\alpha^{(2)} + \cdots + p_D^{(n)}\alpha^{(n)} \quad (6)$$

where p_D^n = polynomial coefficient for the nth degree determined through least-square fitting; and $p_D^0 = C_D(\alpha_0)$ is the coefficient at initial AoA. Therefore, the wind static loads and buffeting force can be rewritten as the polynomial expansion of structural deformation. The derivative of C_D with respect to AoA is

$$C_{D'}(\alpha_0 + \alpha) \approx \mathcal{P}_D^n(\alpha_0 + \alpha) = p_D^{(1)} + 2p_D^{(2)}\alpha^1 + \cdots + np_D^{(n)}\alpha^{n-1} \quad (7)$$

In a similar fashion, the other two aerodynamic forces can be also expanded as Taylor series

$$F_s(U, d) = \frac{1}{2}\rho U^2 \begin{bmatrix} B & & \\ & B & \\ & & B^2 \end{bmatrix} \left\{ \begin{bmatrix} p_D^{(0)} \\ p_L^{(0)} \\ p_M^{(0)} \end{bmatrix} + \begin{bmatrix} p_D^{(1)} \\ p_L^{(1)} \\ p_M^{(1)} \end{bmatrix}\alpha \right.$$

$$\left. + \begin{bmatrix} p_D^{(2)} \\ p_L^{(2)} \\ p_M^{(2)} \end{bmatrix}\alpha^2 + \cdots + \begin{bmatrix} p_D^{(n)} \\ p_L^{(n)} \\ p_M^{(n)} \end{bmatrix}\alpha^n \right\} \quad (8)$$

$$F_b(U, d) = \frac{1}{2}\rho U^2 \begin{bmatrix} B & & \\ & B & \\ & & B^2 \end{bmatrix} \left\{ \begin{bmatrix} 2p_D^{(0)} & p_L^{(0)} + p_D^{(1)} \\ 2p_L^{(0)} & p_D^{(0)} + p_L^{(1)} \\ 2p_M^{(0)} & p_M^{(1)} \end{bmatrix} \right.$$

$$+ \begin{bmatrix} 2p_D^{(1)} & p_L^{(1)} + 2p_D^{(2)} \\ 2p_L^{(1)} & p_D^{(1)} + 2p_L^{(2)} \\ 2p_M^{(1)} & 2p_M^{(2)} \end{bmatrix}\alpha + \begin{bmatrix} 2p_D^{(2)} & p_L^{(2)} + 3p_D^{(3)} \\ 2p_L^{(2)} & p_D^{(2)} + 3p_L^{(3)} \\ 2p_M^{(2)} & 3p_M^{(3)} \end{bmatrix}\alpha^2$$

$$+ \cdots + \begin{bmatrix} 2p_D^{(n)} & p_L^{(n)} + (n+1)p_D^{(n+1)} \\ 2p_L^{(n)} & p_D^{(n)} + (n+1)p_L^{(n+1)} \\ 2p_M^{(n)} & (n+1)p_M^{(n+1)} \end{bmatrix}\alpha^n \right\}$$

$$\times \begin{bmatrix} \dfrac{u(x,t)}{U}\chi_u(n) \\ \dfrac{w(x,t)}{U}\chi_w(n) \end{bmatrix} \quad (9)$$

In the generalized modal coordinates, the bridge deck rotation α can be expanded as follows:

$$\alpha = \theta + \frac{\dot{h} - 0.5B\dot{\theta}}{U}$$
$$= \sum_{j=1}^{L}\phi_{j,\theta}q_j + B\frac{\phi_{j,h} - 0.5\phi_{j,\theta}}{U}\dot{q}_j = \sum_{j=1}^{L}\phi_{j,\theta}q_j + \psi_j\dot{q}_j \quad (10)$$

where L = number of selected modes in reduced-order modeling; $\phi_{j,\theta}$ = rotational part of selected mode shape; $\phi_{j,\theta}$ = vertical motion part; and q_j = deformation in generalized modal coordinates.

In this study, the nonlinear effect from torsional aerostatic deformation is considered, and other motion items are still evaluated as a small number. Therefore $\alpha \approx \theta$ for high-order terms. The second power of θ in terms of generalized coordinates is

$$\alpha^2 = \left[\theta + \frac{\dot{h} - 0.5B\dot{\theta}}{U}\right]^2 \approx \theta^2 = \left[\sum_{j=1}^{L}\varphi_{j,\theta}q_j\right]^2 = [q_1 \quad q_2 \quad \cdots \quad q_L]$$

$$\times \begin{bmatrix} \varphi_{1,\theta}\varphi_{1,\theta} & \varphi_{1,\theta}\varphi_{2,\theta} & \cdots & \varphi_{1,\theta}\varphi_{L,\theta} \\ \varphi_{2,\theta}\varphi_{1,\theta} & \varphi_{2,\theta}\varphi_{2,\theta} & \cdots & \varphi_{2,\theta}\varphi_{L,\theta} \\ \vdots & \vdots & \ddots & \vdots \\ \varphi_{L,\theta}\varphi_{1,\theta} & \varphi_{L,\theta}\varphi_{2,\theta} & \cdots & \varphi_{L,\theta}\varphi_{L,\theta} \end{bmatrix} \begin{bmatrix} q_1 \\ q_2 \\ \vdots \\ q_L \end{bmatrix} = \Phi_{jk}^{(2)}q_jq_k$$

$$(11)$$

Similarly, the third power of θ is

$$\theta^3 = \Phi_{jkm}^{(3)}q_jq_kq_m \quad (12)$$

Next, the generalized aerostatic force for the ith mode is

$$\hat{F}_{s,i} = \int_0^l \Phi_i^T F_s dx = \int_0^l \left[\, B\phi_{i,p}^T \quad B\phi_{i,ha}^T \quad \phi_{i,\theta}^T \,\right] \frac{\rho U^2}{2} \begin{bmatrix} B & & \\ & B & \\ & & B^2 \end{bmatrix} \left\{ \left\{ \begin{bmatrix} p_D^{(0)} \\ p_L^{(0)} \\ p_M^{(0)} \end{bmatrix} + \begin{bmatrix} p_D^{(1)} \\ p_L^{(1)} \\ p_M^{(1)} \end{bmatrix} \alpha + \begin{bmatrix} p_D^{(2)} \\ p_L^{(2)} \\ p_M^{(2)} \end{bmatrix} \alpha^2 + \cdots + \begin{bmatrix} p_D^{(n)} \\ p_L^{(n)} \\ p_M^{(n)} \end{bmatrix} \alpha^n \right\} dx$$

$$= \frac{1}{2}\rho U^2 B^2 \int_0^l \left\{ \begin{array}{c} \left[\, \phi_{i,p}^T \quad \phi_{i,h}^T \quad \phi_{i,\theta}^T \,\right] \begin{bmatrix} p_D^{(0)} \\ p_L^{(0)} \\ p_M^{(0)} \end{bmatrix} + \left[\, \phi_{i,p}^T \quad \phi_{i,h}^T \quad \phi_{i,\theta}^T \,\right] \begin{bmatrix} p_D^{(1)} \\ p_L^{(1)} \\ p_M^{(1)} \end{bmatrix} \alpha + \\[20pt] \left[\, \phi_{i,p}^T \quad \phi_{i,h}^T \quad \phi_{i,\theta}^T \,\right] \begin{bmatrix} p_D^{(2)} \\ p_L^{(2)} \\ p_M^{(2)} \end{bmatrix} \alpha^2 + \cdots + \left[\, \phi_{i,p}^T \quad \phi_{i,h}^T \quad \phi_{i,\theta}^T \,\right] \begin{bmatrix} p_D^{(n)} \\ p_L^{(n)} \\ p_M^{(n)} \end{bmatrix} \alpha^n \end{array} \right\} dx$$

$$= \frac{1}{2}\rho U^2 B^2 \int_0^l \left[\hat{p}_i^{(0)} + \hat{p}_i^{(1)}\alpha + \hat{p}_i^{(2)}\alpha^2 + \cdots + \hat{p}_i^{(n)}\alpha^n\right] dx$$

$$= \frac{1}{2}\rho U^2 B^2 \left[\hat{p}_i^{(0)} + \hat{p}_i^{(1)}\Phi_j^{(1)}q_j + \hat{p}_i^{(2)}\Phi_{jk}^{(2)}q_j q_k + \cdots + \hat{p}_i^{(n)}\Phi_{jkm,\dots}^{(n)}(q_j q_k q_m, \dots)\right] + \frac{1}{2}\rho U^2 B^2 \hat{p}_i^{(1)}\psi_j \dot{q}_j \tag{13}$$

where

$$\hat{p}_i^{(n)} = \left[\, \phi_{i,p}^T \quad \phi_{i,h}^T \quad \phi_{i,\theta}^T \,\right] \begin{bmatrix} p_D^{(n)} \\ p_L^{(n)} \\ p_M^{(n)} \end{bmatrix}$$

Assembling the aerostatic force for each component, the generalized aerostatic force vector is

$$\hat{F}_s = \hat{F}_0 + \hat{F}_{ek}(q) + \hat{F}_{ec}(\dot{q}) \tag{14}$$

where $\hat{F}_0 = \frac{1}{2}\rho U^2 B^2 [\, \hat{p}_1^{(0)} \quad \hat{p}_2^{(0)} \quad \cdots \quad \hat{p}_n^{(0)} \,]^T$ is the initial aerostatic force without structural deformation; $\hat{F}_{ek}(q)$ = aerodynamic-induced stiffness; and $\hat{F}_{ec}(\dot{q})$ = aerodynamic induced damping.

Next, the generalized buffeting force for the ith mode is

$$\hat{F}_{b,i} = \frac{1}{2}\rho U^2 B^2 \left[\check{p}_i^{(0)} + \check{p}_i^{(1)}\Phi_j^{(1)}q_j \right.$$
$$\left. + \check{p}_i^{(2)}\Phi_{jk}^{(2)}q_j q_k + \cdots + \check{p}_i^{(n)}\Phi_{jkm\dots}^{(n)}(q_j q_k q_m, \dots)\right] \begin{bmatrix} \hat{u} \\ \hat{w} \end{bmatrix} \tag{15}$$

where

$$\check{p}_i^{(n)} = \left[\, \phi_{i,p}^T \quad \phi_{i,h}^T \quad \phi_{i,\theta}^T \,\right] \begin{bmatrix} 2p_D^{(n)} & p_L^{(n)} + (n+1)p_D^{(n+1)} \\ 2p_L^{(n)} & p_D^{(n)} + (n+1)p_L^{(n+1)} \\ 2p_M^{(n)} & (n+1)p_M^{(n+1)} \end{bmatrix}$$

Let $\hat{u}_i$ and $\hat{w}_i$ denote the normalized turbulence $u(t)/U$ and $w(t)/U$, including the chordwise admittance and spanwise turbulence coherence effects for the ith mode

$$\hat{u}_i = \frac{u(t)}{U}\chi_u(n)\frac{\iint_0^l \phi_i(x_1)\phi_i(x_2)\exp\left(-\frac{nC_x|x_1-x_2|}{U}\right)dx_1 dx_2}{\iint_0^l \phi_i(x_1)\phi_i(x_2)dx_1 dx_2} \tag{16}$$

The hybrid expression of time and frequency in Eq. (16) can be transformed to the fully frequency domain by Fourier transformation.

From the viewpoint of stochastic vibration, the normalized turbulence $\hat{u}$ and $\hat{w}$ can be approximated by two independent filtered Gaussian processes through fitting Eq. (16) in the frequency domain

$$d\hat{u}_i = -\alpha_{u_i}\hat{u}_i dt + \sigma_{u_i}\sqrt{2\alpha_{u_i}}dW_u \tag{17a}$$

$$d\hat{w}_i = -\alpha_{w_i}\hat{w}_i dt + \sigma_{w_i}\sqrt{2\alpha_{w_i}}dW_w \tag{17b}$$

Therefore, the buffeting force can be expressed in the same way

$$\hat{F}_b = P(q)\begin{bmatrix} \hat{u} \\ \hat{w} \end{bmatrix} \tag{18}$$

Finally, the dynamic governing equation considering nonlinear stiffness and nonlinear aerodynamic in generalized coordinates is

$$\hat{M}\ddot{q} + \hat{C}\dot{q} + \hat{K}_e q + \hat{K}_n(q) = \hat{F}_0 + \hat{F}_{ek}(q) + \hat{F}_{ec}(\dot{q}) + P(q)\begin{bmatrix} \hat{u} \\ \hat{w} \end{bmatrix} \tag{19}$$

The preceding generalized motion equation can be expressed as a state-space equation as follows:

$$dQ = A(Q)dt + B(Q)Z(t) \tag{20}$$

where $Q = \left\{ \begin{array}{c} q \\ \dot{q} \end{array} \right\}$, $A(Q) = \begin{bmatrix} \dot{q} \\ -\hat{M}^{-1}\hat{K}(q) - \hat{M}^{-1}\hat{C}\dot{q} \end{bmatrix}$, $B(Q) = \begin{bmatrix} 0 \\ \hat{M}^{-1}P(q) \end{bmatrix}$, $\hat{K}(q) = \hat{K}_e q + \hat{K}_n(q) - \hat{F}_{ek}(q) - \hat{F}_{ec}(\dot{q})$, $Z(t) = \begin{bmatrix} \hat{u} \\ \hat{w} \end{bmatrix}$.

Description of Bridge Structural Model

A virtual long-span bridge was constructed in commercial finite-element software platform ANSYS version 14.0. In this study, a long-span bridge example with a main span of 5,000 m and a deck width of 50 m was employed. The bridge is illustrated in Fig. 2. A 5,000-m span is the longest bridge analyzed in the current field of bridge engineering (Ge et al. 2018), and its engineering practicability was discussed by Xia et al. (2021).

Tensile link (LINK180) elements are employed to model the suspended cables and hangers. The main bridge girder is modeled using Euler beam elements (BEAM188) and connected to hangers through a rigid "fish-bone" framework (Ko et al. 1998). The bridge girders and suspension cables was discretized at the hanger locations.
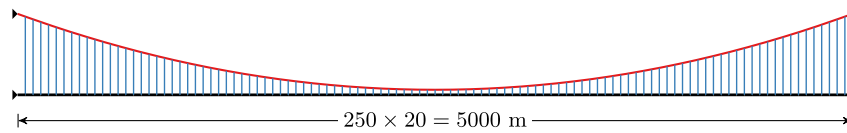
Fig. 2. FEM model of a virtual bridge.

Table 1. Structural parameters for the conceptual 5,000-m-span bridge

Parameters	Values	Parameters	Values
Main span	5,000	Area of bridge section (m^2)	1.11
Sag-span ratio	1/11	Area moment of inertia, $I_x/I_y/I_z$ (m^4)	16.82/6.41/315
Deck width, B (m)	50	Area of main cable (m^2)	2.47
Deck thickness, D (m)	2.5	Hanger	Massless and infinite stiffness
Mass per unit length, M (kg/m)	48,000	Structural damping ratio	0.005
Mass moment of inertia along longitudinal axis per unit length, I (kg · m^2/m)	2,800,000	Air density, ρ (kg/m^3)	1.25
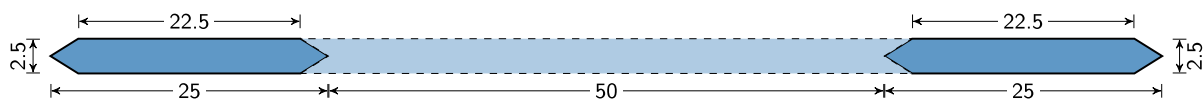
Fig. 3. Geometries of bridge section (unit: m).

For the boundary conditions, the two ends of both bridge girder and main cables were all simply supported (translational displacement along three directions is restricted). Thus, the bridge towers were omitted. The main parameters of this virtual bridge are given in Table 1.

As in the original analysis by Ge et al. (2018), an ultrawide center-slotted twin-box sectional model was employed as the prototype bridge section in this study. The height was 2.5 m and the central slot width was 50 m. The detailed geometries of the bridge section are depicted in Fig. 3. The 5,000-m-span bridge and its associated section shape proposed in this study are only the conceptual and preliminary study, and there were no barriers installed on the sectional model.

Based on the section shape geometries, this sectional model was tested in the wind tunnel to measure the aerostatic coefficients. The measured drag coefficient C_D, lift coefficient C_L, and pitch coefficient C_M for the AoA α in the range ($-12°$ to $12°$) are plotted as scatters in Fig. 4. To smooth the aerostatic loads calculated in the latter steps, third-order polynomial was used to fit the C_D, C_L, and

C_M coefficient as in Eq. (21). The formula used to fit C_L and C_M are the same, but the coefficients are different, as in Eqs. (22) and (23). The values of C_D, C_L, and C_M from fitted formulas are also plotted in Fig. 4

$$C_D(\alpha) = -0.9249\alpha^3 + 6.6989\alpha^2 - 0.1851\alpha + 0.1579 \quad (21)$$

$$C_L(\alpha) = -32.5465\alpha^3 - 0.3901\alpha^2 + 3.4192\alpha - 0.0638 \quad (22)$$

$$C_M(\alpha) = 1.1203\alpha^3 - 1.4492\alpha^2 + 0.2135\alpha + 0.0111 \quad (23)$$

Reduced-Order Modeling of Long-Span Bridge Structural Stiffness and Aerostatic Loads

According to the finite-element method established by Cheng et al. (2002) and the long-span bridge properties described in the previous section, the aerostatic bridge deformation analysis can be performed for prescribed initial wind AoA. Fig. 5 shows the bridge aerostatic displacements at the middle span $x = L/2$ along horizontal p, vertical h, and torsional θ directions for various wind
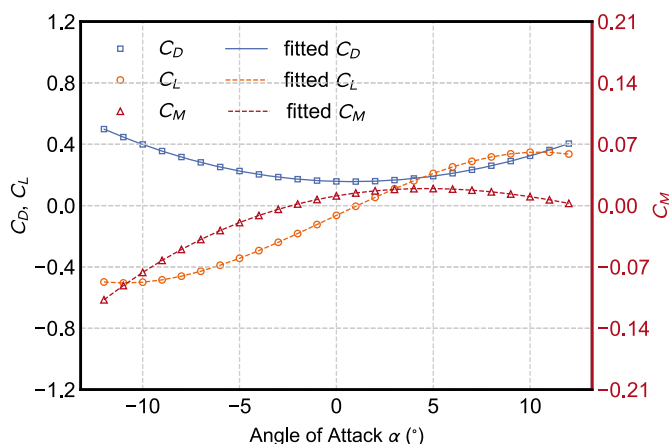

Fig. 4. Aerostatic coefficients of bridge deck.
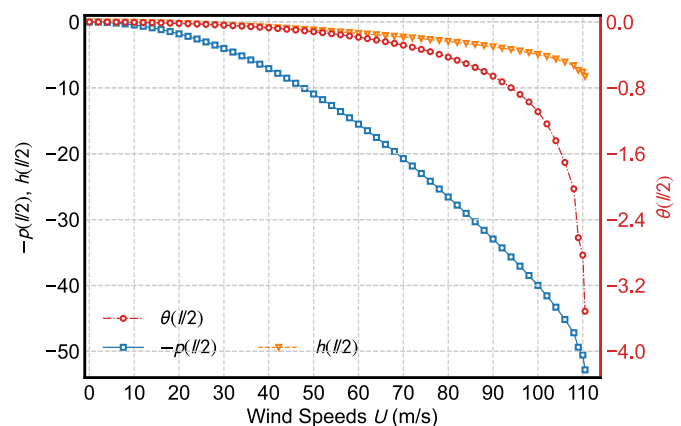

Fig. 5. Three-directional bridge girder deflection at middle span for various wind speeds when initial AoA $\alpha_0 = 3°$.
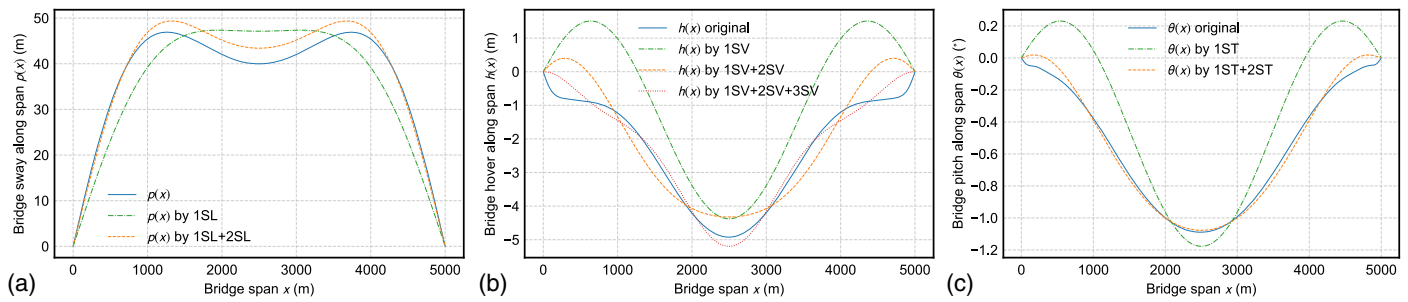
Fig. 6. Reduced-order modeling of bridge aerostatic deformation ($U = 100$ m/s): (a) sway; (b) hover; and (c) pitch.

speeds U with initial AoA $\alpha_0 = 3°$. The units for p and h are meters and the unit for θ is degrees. The displacement curves showed that aerostatic buckling for $\alpha_0 = 3°$ is a typical limit-point buckling (Leahu-Aluas and Abed-Meraim 2011). When wind speed $U \geq 100$ m/s, the structural rotational and vertical deformation grew dramatically. Finally, the FEM model cannot converge to a stable equilibrium point when $U \geq 110$ m/s.

The along-span bridge girder deflection shapes when the wind speed is $U = 100$ m/s in sway, hover, and pitch directions are plotted in Figs. 6(a–c), respectively. Normally, the overall girder deflection shape can be decomposed into low-dimensional reduced-order modes (Mignolet et al. 2013). Because the purpose of this study is analyzing the wind-induced random vibration, the dynamic modes derived from the general eigenvalue decomposition of K to M were employed in this study. The modes frequencies and associated modal shapes are presented in Table 2. The approximate girder deflection shape by selective dynamic modes are plotted as a dashed line in Figs. 6(a–c).

Table 2. Modal shape and frequency of first 14 modes

Number	Frequency	Mode shape
1	0.025	1SL
2	0.039	1ASL
3	0.048	2SL
4	0.052	1ASV
5	0.066	2ASL
6	0.069	1SV
7	0.071	1AST
8	0.085	3ASL
9	0.086	3SL
10	0.092	1ST
11	0.094	2SV
12	0.102	2ASV
13	0.121	2ST
14	0.127	4ASL

Note: L = lateral; V = vertical; T = torsional; S = symmetric; AS = asymmetric; and number = mode order.

Because the bridge girder deflection shape in three directions is symmetric, only symmetric dynamic modes were used to approximate the girder motion. The asymmetric modes still can be excited by turbulence, but they do not interact with aerostatic deflection. Figs. 6(a–c) show that 1 lateral symmetric (SL) and 2 SL, 1 vertical symmetric (VS), 2VS, and 3VS, and 1 torsional symmetric (TS) and 2TS can have a good approximation of bridge girder deflection with sufficient accuracy. However, in order to balance the computational burden and simulation accuracy, only SL1, VS1, VS2, and TS1 are considered in the following study about nonlinear wind-induced vibration.

If only the static part of Eq. (5) is considered, the aerostatic equilibrium in reduced order is

$$\hat{K}_e q + \hat{K}_n(q) = \hat{F}_s = \hat{F}_0 + \hat{K}_a(q) \qquad (24)$$

where $\hat{F}_0$ and $\hat{K}_a(q)$ can be determined by Eq. (14); and $\hat{K}_e$ is the diagonal matrix composed by the square of the circular frequency of selected modes if the modes shapes are a normalized mass matrix ($\hat{M}$ is a unitary matrix).

$\hat{K}_n(q)$ normally cannot be directly determined through the finite-element method; therefore, several indirect methods were developed (Mignolet et al. 2013). In this study, the displacement-based indirect method is employed in this study to determine the nonlinear stiffness coefficients. The basic logic of the displacements-based indirect method is applying the generalized displacement q_i with different amplitudes onto the FEM model and collecting the reaction force on each girder node then covering the generalized mode forces. Next, the nonlinear stiffness can be determined through the constitution established by the generalized displacements and generalized forces.

Nevertheless, unlike the mode decomposition of linear stiffness structure, the nonlinear stiffness is coupled among the selected modes. Thus, all the stiffness matrix coefficients for the considered modes should be analyzed together rather than one-by-one as for linear stiffness.
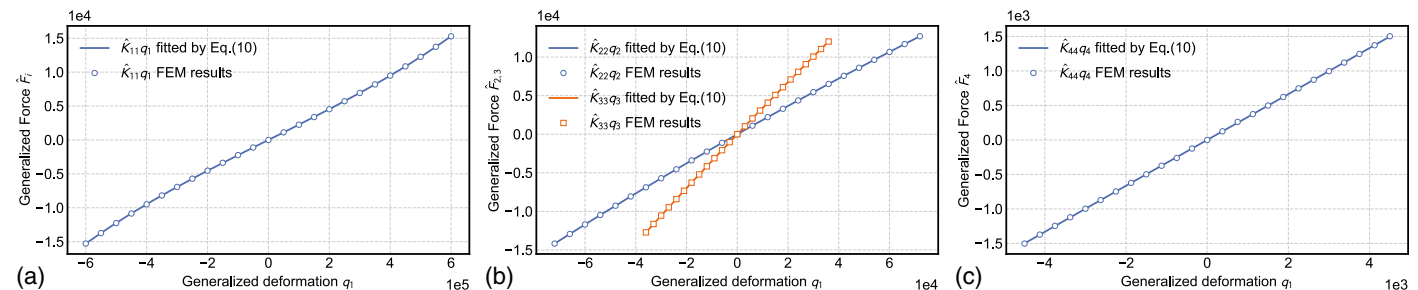

Fig. 7. Generalized forces and displacements relationship: (a) Mode 1SL; (b) Mode 1SV and 2SV; and (c) Mode 1ST.
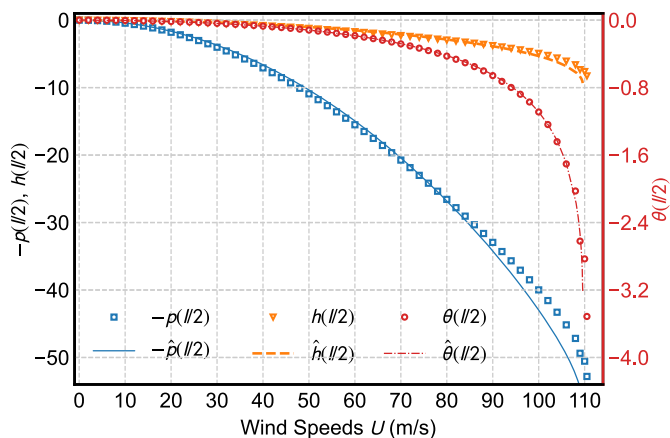
Fig. 8. Validation of nonlinear stiffness in reduced-order model about aerostatic deformation.

Because of the complexity of the four modes' coupled nonlinear stiffness, only slices of the stiffness relationship along each corresponding mode are displaced in Figs. 7(a–c). It can be noticed that for the hover modes 1SV and 2SV and pitch mode 1ST, the stiffness was almost linear within the analyzed displacement range. However, the sway mode 1SL had moderate stiffness nonlinearity, which is nonnegligible for the aeroelastic deformation analyzed in the following content.

In order to validate the nonlinear stiffness matrix and reduced-order expression of aerostatic force, the aerostatic deformation calculated by the reduced-order methods is compared against the results from FEM in Fig. 8. Besides small differences at large wind speed, the great match between the two results shows that the nonlinear stiffness and aerostatic force can be modeled correctly by the reduced-order model.

Furthermore, the interaction between pitch mode and deflection mode shape is insignificant. On the other hand, the aerodynamic nonlinearity on both aerostatic $\hat{\boldsymbol{F}}_s$ and buffeting force $\hat{\boldsymbol{F}}_b$ depend
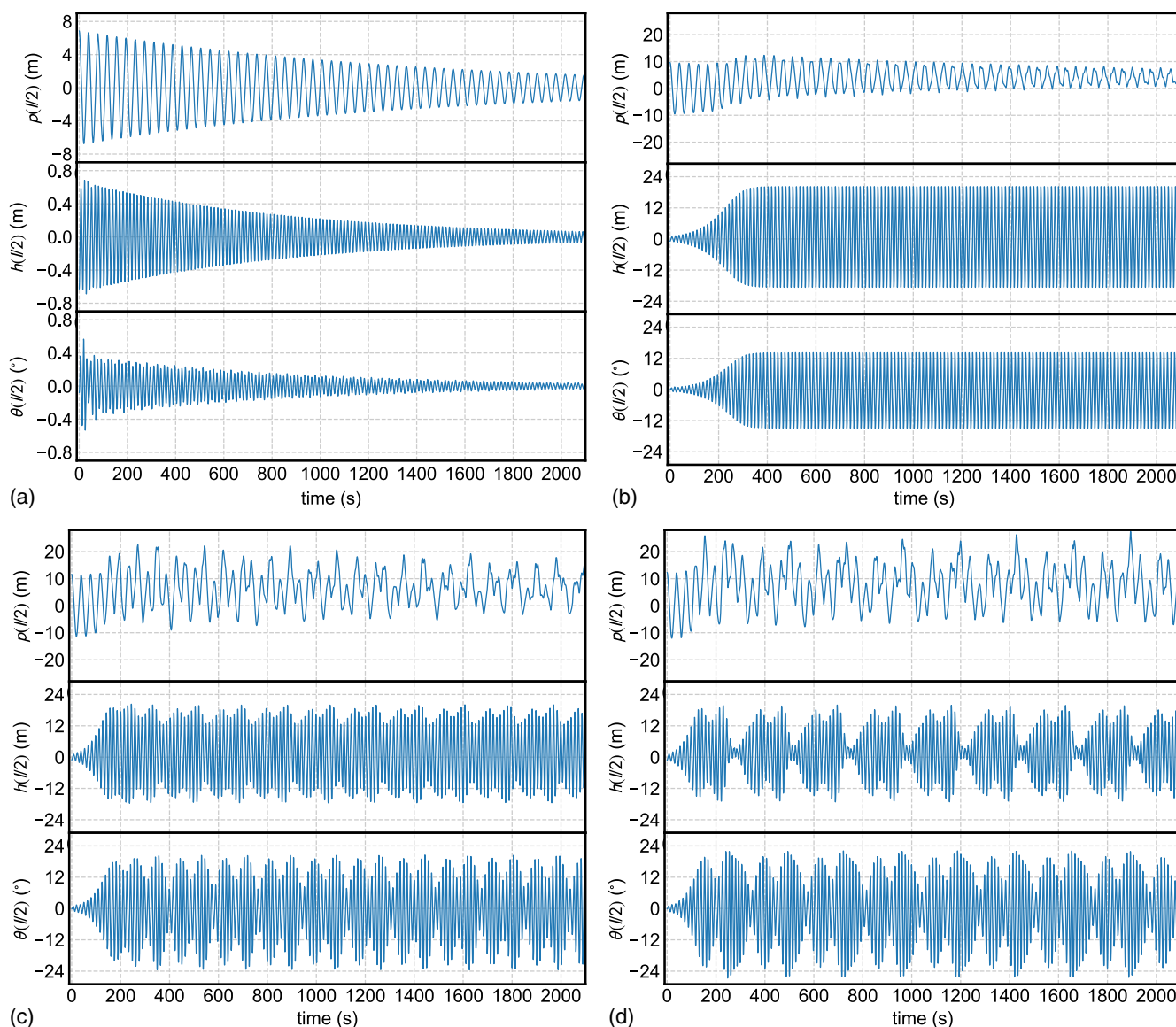

Fig. 9. Various aeroelastic responses at different wind speeds: (a) $U = 54$ m/s; (b) $U = 64$ m/s; (c) $U = 70$ m/s; and (d) $U = 72$ m/s.

solely on the pitch deformation. Therefore, the wind-induced non-linear random vibration can be further reduced to the pitch modes only. Next, according to the wind-induced pitch deformation, the sway and hover vibration can be calculated afterward as a deterministic problem. Because the second step is trivial, the remaining part of this study will focus on pitch motion only.

Wind-Induced Bridge Aeroelastic Response

After the determination of structural parameters through reduced-order modelling (ROM) method and aeroelastic parameters through quasi-steady theory, the aeroelastic response without turbulence effects is first carried out in this study. Without the external turbulence effect, the state-space equation is reduced as follows:

$$dQ = A(Q)dt \qquad (25)$$

After assembling all components in Eq. (20), the structural vibration can be simulated by a modified Rosenbrock formula of order 2 (Kaps and Rentrop 1979), which can solve stiff ordinary differential equations when strong nonlinearity is exhibited in Eq. (20).

The initial condition for each simulation is that the structural displacements for each mode are perturbed randomly from the static equilibrium displacements. Under different wind speeds, the structure response will decay to zero or self-excite to certain amplitudes depending on the aeroelastic effect on structural vibration.

Fig. 8 shows different aeroelastic response at four wind speeds, and the aerostatic displacement calculated in Fig. 8 are excluded, which means the aeroelastic response starts from equilibrium points. In Fig. 9(a), the displacements at three directions all decayed to zero from initial amplitudes, which means the aeroelastic instability will not occur for $U \leq 54$ m/s. For $U > 54$ m/s, the structural response was self-excited and increasing initially, but the response then reached a stable amplitudes and vibrated continuously because of the strong aeroelastic nonlinearity. Taking $U = 64$ m/s in Fig. 9(b) as example, because the the wind caused lift and pitching force reduce for large AoA, the structural response will not increase after reaching a certain amplitude. This phenomena is also called limit-cycle oscillation (Strogatz 2018).

When $U = 70$ m/s, a vibration beating phenomenon appeared due to the modes coupling due to the aerodynamic stiffness. As wind speeds increased to $U = 72$ m/s, the vibration beating phenomenon became more obvious, and the torsional vibration amplitude increased but the hovering (vertical) vibration amplitude decreased slightly because of more obvious beat vibration phenomena. For Figs. 9(b–d), the lateral vibration was more like a forced motion because of the drag force varying with effective AoA.

Fig. 10 shows a typical flutter instability when $U = 74$ m/s. Fig. 11 plots the relationship between maximum amplitudes of three-directional response. After $U = 54$ m/s, soft fluttering occurred and the amplitudes increased with wind speeds, except the vertical direction was reduced because of beating vibration. For $U > 72$ m/s, the bridge structure cannot converge to a stable amplitudes, and Fig. 10 shows a typical flutter instability when $U = 74$ m/s.

At last, the aeroelastic response amplitudes were also calculated by FEM. The nonlinear aeroelastic force based on quasi-steady theory was implemented in the ANSYS platform. The standard time integration method was employed, and at each time step, the effective angle of attack and structural moving velocity were collected to derive the instantaneous aeroelastic force. Therefore, the structural responses was calculated step-by-step in the time domain. The responses derived by FEM and the ROM method proposed in this study are compared in Fig. 12, in which the results from the ROM
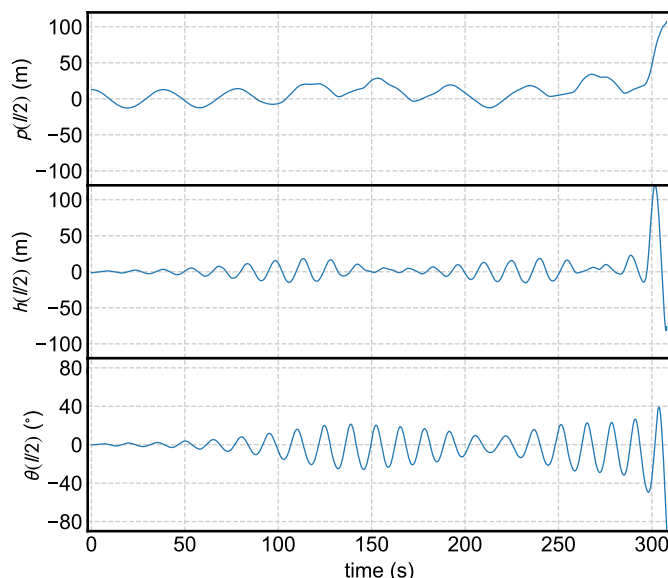

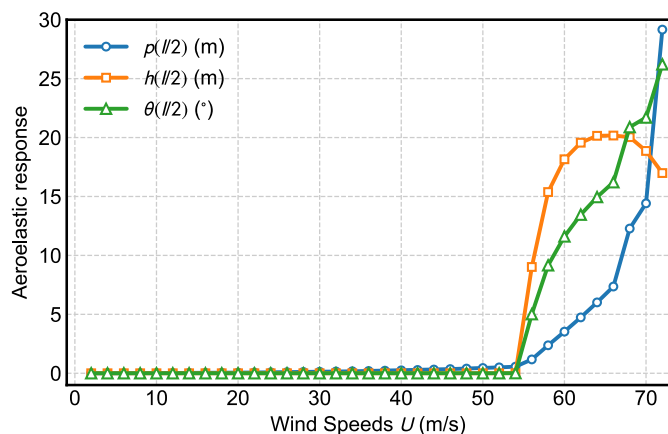**Fig. 10.** Flutter instability occurs at $U = 74$ m/s.

Fig. 11. Relationship between three-directional response amplitudes and wind speeds.
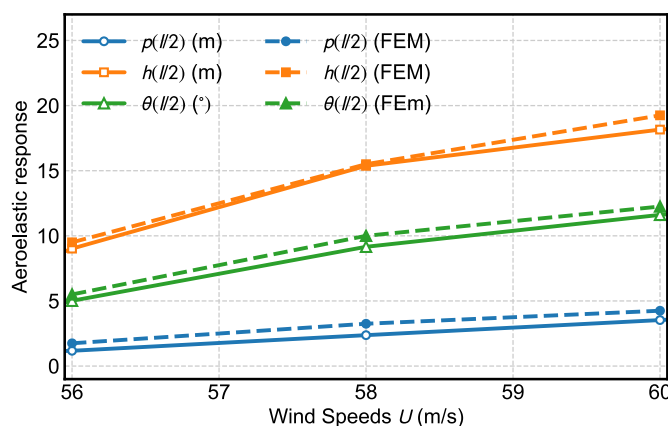

Fig. 12. Validation of proposed aeroelastic model through comparison with FEM results.
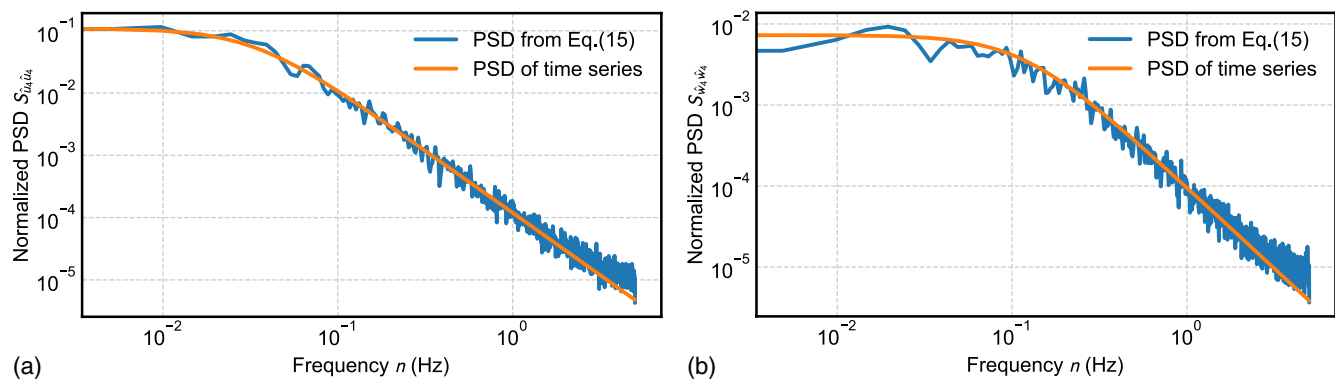
Fig. 13. Comparison of generated turbulence PSD to target PSD in Eq. (16): (a) along-wind component $\hat{u}4$ for Mode 4; and (b) vertical component $\hat{w}4$ for Mode 4.
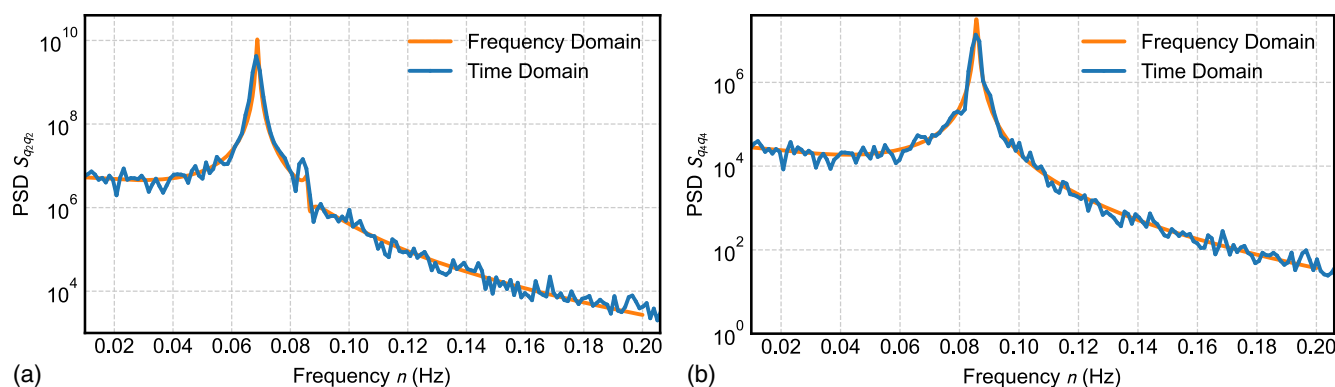

Fig. 14. Comparison of PSD of time simulation results against standard frequency domain: (a) Mode 2; and (b) Mode 4.

method roughly matched the FEM results. However, the FEM results were generally larger than the ROM method because of higher-mode effects, which is cannot be included in the ROM method.

Wind-Induced Bridge Buffeting Response Considering Structural and Aeroelastic Nonlinearity

The equivalent turbulence components $\hat{u}_i$ and $\hat{w}_i$ in the frequency domain can be found in Eq. (16). Then, the time-domain implementation of $\hat{u}_i(t)$ and $\hat{w}_i(t)$ is generated using Shinozuka's spectrum superposition method (Shinozuka 1974) and accelerated by fast Fourier transformation (Deodatis 1996). Fig. 13 plots the power spectral density (PSD) of simulated the turbulence and target spectrum to validate simulation accuracy.

Then, the simulated turbulence is imported into the Eq. (20), and the structural vibration time series can also be calculated by the aforementioned time integration methods. In order to validate the accuracy of the aforementioned established vibration equations, the standard frequency domain methods of Jones and Scanlan (2001) without consideration of self-excited aeroelastic force were performed to compare the result. Only the linear part in Eq. (5) was transformed into frequency domain in the calculation procedure. The results for Mode 2 and Mode 4 are plotted in Fig. 14, and other modes are omitted for brevity. The great match in both Figs. 14(a and b) confirms the correctness of vibration equation in Eq. (20) and the implementation of the time-domain simulation.

After verification of the linearized ROM methods, the high-order nonlinear terms for both aeroelasticity and structural stiffness were added to the dynamic model to simulate the wind-induced structural response with the turbulence effect. Similar to the aeroelastic response in Fig. 9, $U = 54$, 64, 70, and 72 m/s were taken as examples in Fig. 15. For the nonflutter case with $U = 54$ m/s, the vibration responses in Fig. 15(a) are a typical random buffeting response. For the soft flutter case with $U = 64$ m/s, vertical and torsional responses can be considered as the summation of typical limit-cycle oscillations and random buffeting, and the overall averaged response were roughly similar to the pure aeroelastic response in Fig. 9(b) because the self-excited wind loads dominated the response, and buffeting force was just small perturbation from limit-cycle oscillations. In contrast, the lateral responses in both Figs. 15(a and b) were much larger due to the lower frequency of lateral modes.

For the higher wind speed $U = 70$ m/s in Fig. 15(c), the vibration became unstable, and when the lateral vibration amplitude was beyond 60 m, the time-integration program could not converge, which means it is difficult for structure to return the equilibrium point at such large vibration. For the higher wind speed $U = 72$ m/s in Fig. 15(d), the divergence occurred very early, and structure also could not converge for $U > 72$ m/s. Fig. 16 summarizes the midspan three-directional displacement at different wind speeds.
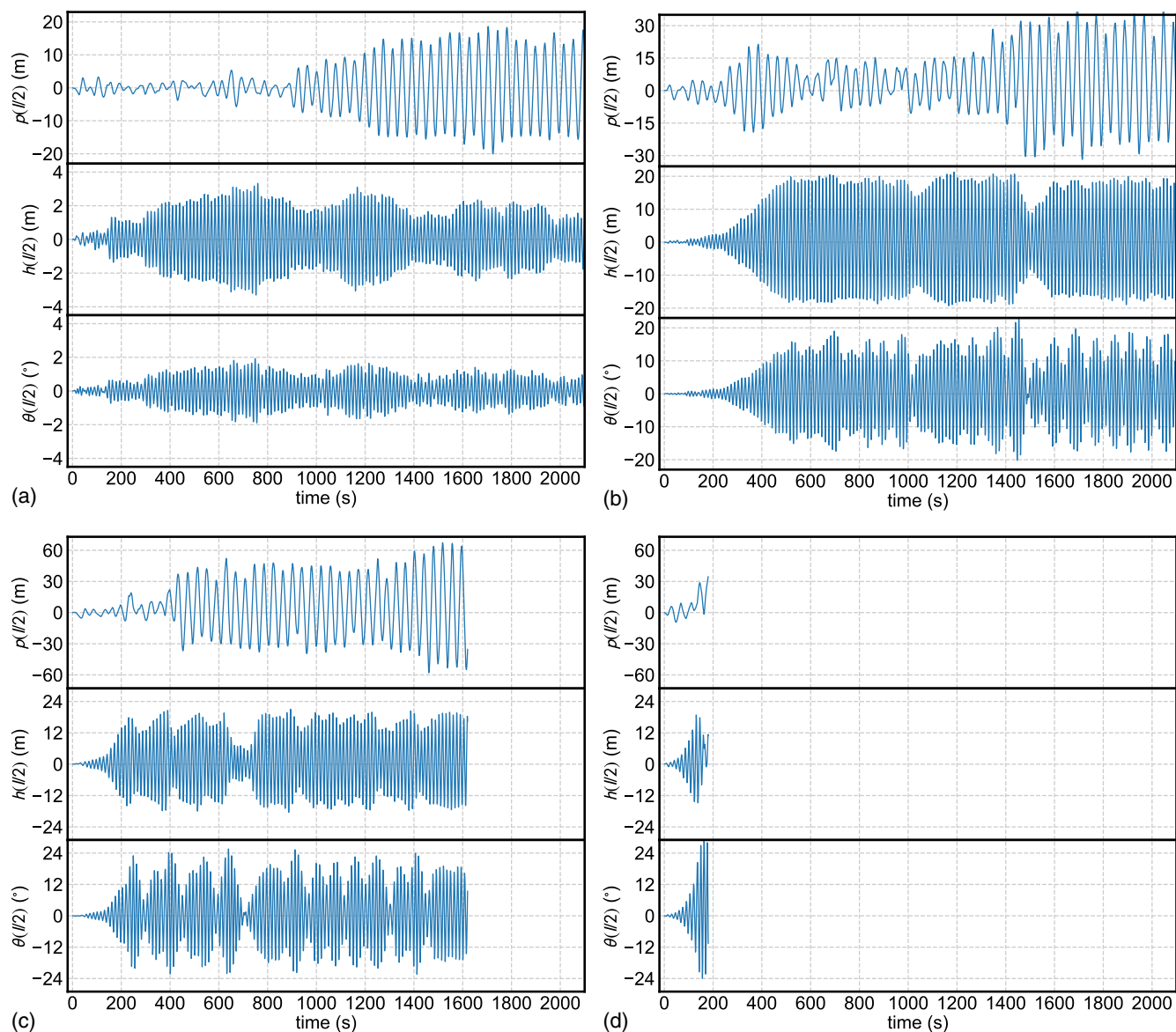
Fig. 15. Various bridge buffeting responses at different wind speeds: (a) $U = 54$ m/s; (b) $U = 64$ m/s; (c) $U = 70$ m/s; and (d) $U = 72$ m/s.
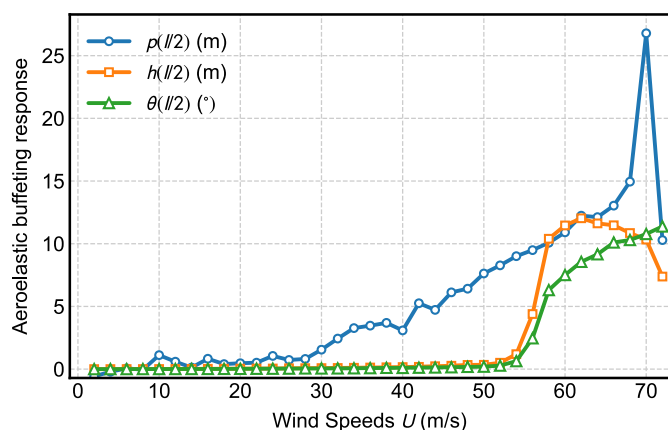

Fig. 16. Relationship between three-directional buffeting response RMS amplitudes and wind speeds.

Conclusions

In this study, a reduced-order modeling method was proposed to study the wind-induced random buffeting vibration considering both structural and aerodynamic nonlinearity. First, a dynamic model–based vibration formula was derived through expanding the structural and aerodynamic nonlinearity into polynomial series. The static part of the formula was validated through the comparison against the finite-element methods results. The aeroelastic force is based on classical quasi-steady theory considering the aerodynamic nonlinearity caused by varying effective angle of attack. The structural stiffness was reduced to targeted modes by indirect reduced-order modeling. At first, the structural wind-induced nonlinear aeroelastic model was built by assembling the aeroelastic and structural parts into one state-space dynamic model, and the responses were calculated by a time-integration algorithm.

The accuracy of the proposed ROM method for the aerostatic and aeroelastic responses was validated through comparison with

the FEM result. For low wind speeds, the structural response decayed to the original equilibrium states. When wind speeds were larger than the critical value, the response would not decay to zero but continuously vibrated at constant amplitudes (limit-cycle oscillation). Next, for a higher wind speeds, the beat vibration phenomena appeared because of multimode interaction. When wind speeds were larger than the unstable critical value, bridge flutter occurred onsite because the aeroelastic response was constantly growing.

The aeroelastic responses calculated by the proposed ROM method were compared against the FEM result to validate its accuracy. Next, the turbulent wind field was generated numerically, and the structural random buffeting response was also calculated by the time-integration method. In vertical and torsional direction, the buffeting effect only slightly changed the vibration amplitude; however, in the lateral direction, the buffeting response was much larger than the pure aeroelastic response, which caused the early instability of bridge structures at lower wind speed.

Data Availability Statement

All data, models, and code generated or used during the study appear in the published article.

Acknowledgments

References

Amman, O. H., T. von Kármán, and G. B. Woodruff. 1941. *The failure of the Tacoma Narrows Bridge*. Washington, DC: Federal Works Agency.

Arena, A., and W. Lacarbonara. 2012. "Nonlinear parametric modeling of suspension bridges under aeroelastic forces: Torsional divergence and flutter." *Nonlinear Dyn.* 70 (4): 2487–2510. https://doi.org/10.1007/s11071-012-0636-3.

Barni, N., O. Øiseth, and C. Mannini. 2021. "Time-variant self-excited force model based on 2D rational function approximation." *J. Wind Eng. Ind. Aerodyn.* 211 (Apr): 104523. https://doi.org/10.1016/j.jweia.2021.104523.

Borri, C., and C. Costa. 2004. "Quasi-steady analysis of a two-dimensional bridge deck element." *Comput. Struct.* 82 (13–14): 993–1006. https://doi.org/10.1016/j.compstruc.2004.03.019.

Cao, S., Y. Tamura, N. Kikuchi, M. Saito, I. Nakayama, and Y. Matsuzaki. 2009. "Wind characteristics of a strong typhoon." *J. Wind Eng. Ind. Aerodyn.* 97 (1): 11–21. https://doi.org/10.1016/j.jweia.2008.10.002.

Chen, X., M. Matsumoto, and A. Kareem. 2000. "Time domain flutter and buffeting response analysis of bridges." *J. Eng. Mech.* 126 (1): 7–16. https://doi.org/10.1061/(ASCE)0733-9399(2000)126:1(7).

Cheng, J., J.-J. Jiang, R.-C. Xiao, and H.-F. Xiang. 2002. "Nonlinear aerostatic stability analysis of Jiang Yin Suspension Bridge." *Eng. Struct.* 24 (6): 773–781. https://doi.org/10.1016/S0141-0296(02)00006-8.

Costa, C., C. Borri, O. Flamand, and G. Grillaud. 2007. "Time-domain buffeting simulations for wind–bridge interaction." *J. Wind Eng. Ind. Aerodyn.* 95 (9–11): 991–1006. https://doi.org/10.1016/j.jweia.2007.01.026.

Cui, W., and L. Caracoglia. 2018a. "A fully-coupled generalized model for multi-directional wind loads on tall buildings: A development of the quasi-steady theory." *J. Fluids Struct.* 78 (Apr): 52–68. https://doi.org/10.1016/j.jfluidstructs.2017.12.008.

Cui, W., and L. Caracoglia. 2018b. "A unified framework for performance-based wind engineering of tall buildings in hurricane-prone regions based on lifetime intervention-cost estimation." *Struct. Saf.* 73 (Jul): 75–86. https://doi.org/10.1016/j.strusafe.2018.02.003.

Davenport, A. G. 1962. "Buffeting of a suspension bridge by storm winds." *J. Struct. Div.* 88 (3): 233–270. https://doi.org/10.1061/JSDEAG.0000773.

Deodatis, G. 1996. "Simulation of ergodic multivariate stochastic processes." *J. Eng. Mech.* 122 (8): 778–787. https://doi.org/10.1061/(ASCE)0733-9399(1996)122:8(778).

Diana, G., D. Rocchi, T. Argentini, and S. Muggiasca. 2010. "Aerodynamic instability of a bridge deck section model: Linear and nonlinear approach to force modeling." *J. Wind Eng. Ind. Aerodyn.* 98 (6–7): 363–374. https://doi.org/10.1016/j.jweia.2010.01.003.

Gao, G., L. Zhu, W. Han, and J. Li. 2018. "Nonlinear post-flutter behavior and self-excited force model of a twin-side-girder bridge deck." *J. Wind Eng. Ind. Aerodyn.* 177 (Jun): 227–241. https://doi.org/10.1016/j.jweia.2017.12.007.

Gao, G., L. Zhu, J. Li, and W. Han. 2020. "Application of a new empirical model of nonlinear self-excited force to torsional vortex-induced vibration and nonlinear flutter of bluff bridge sections." *J. Wind Eng. Ind. Aerodyn.* 205 (Oct): 104313. https://doi.org/10.1016/j.jweia.2020.104313.

Ge, Y., J. Xia, L. Zhao, and S. Zhao. 2018. "Full aeroelastic model testing for examining wind-induced vibration of a 5,000 m spanned suspension bridge." *Front. Built Environ.* 4 (Apr): 20. https://doi.org/10.3389/fbuil.2018.00020.

Hollkamp, J. J., R. W. Gordon, and S. M. Spottswood. 2005. "Nonlinear modal models for sonic fatigue response prediction: A comparison of methods." *J. Sound Vib.* 284 (3–5): 1145–1163. https://doi.org/10.1016/j.jsv.2004.08.036.

Jones, N. P., and R. H. Scanlan. 2001. "Theory and full-bridge modeling of wind response of cable-supported bridges." *J. Bridge Eng.* 6 (6): 365–375. https://doi.org/10.1061/(ASCE)1084-0702(2001)6:6(365).

Kaps, P., and P. Rentrop. 1979. "Generalized runge-kutta methods of order four with stepsize control for stiff ordinary differential equations." *Numer. Math.* 33 (1): 55–68. https://doi.org/10.1007/BF01396495.

Ko, J., S. Xue, and Y. Xu. 1998. "Modal analysis of suspension bridge deck units in erection stage." *Eng. Struct.* 20 (12): 1102–1112. https://doi.org/10.1016/S0141-0296(97)00207-1.

Leahu-Aluas, I., and F. Abed-Meraim. 2011. "A proposed set of popular limit-point buckling benchmark problems." *Struct. Eng. Mech.* 38 (6): 767–802. https://doi.org/10.12989/sem.2011.38.6.767.

Li, K., Y. Han, C. Cai, P. Hu, and C. Li. 2021. "Experimental investigation on post-flutter characteristics of a typical steel-truss suspension bridge deck." *J. Wind Eng. Ind. Aerodyn.* 216 (Sep): 104724. https://doi.org/10.1016/j.jweia.2021.104724.

Liu, S., L. Zhao, G. Fang, C. Hu, and Y. Ge. 2022. "Nonlinear aerodynamic characteristics and modeling of a quasi-flat plate at torsional vibration: Effects of angle of attack and vibration amplitude." *Nonlinear Dyn.* 107 (Feb): 1–25.

Mignolet, M. P., A. Przekop, S. A. Rizzi, and S. M. Spottswood. 2013. "A review of indirect/non-intrusive reduced order modeling of nonlinear geometric structures." *J. Sound Vib.* 332 (10): 2437–2460. https://doi.org/10.1016/j.jsv.2012.10.017.

Muravyov, A. A., and S. A. Rizzi. 2003. "Determination of nonlinear stiffness with application to random vibration of geometrically nonlinear structures." *Comput. Struct.* 81 (15): 1513–1523. https://doi.org/10.1016/S0045-7949(03)00145-7.

Przekop, A., M. S. Azzouz, X. Guo, C. Mei, and L. Azrar. 2004. "Finite element multiple-mode approach to nonlinear free vibrations of shallow shells." *AIAA J.* 42 (11): 2373–2381. https://doi.org/10.2514/1.483.

Shinozuka, M. 1974. "Digital simulation of random processes in engineering mechanics with the aid of FFT technique (fast Fourier transformation)." In *Stochastic problems in mechanics*, 277–286. Berlin: Springer.

Strogatz, S. H. 2018. *Nonlinear dynamics and chaos: With applications to physics, biology, chemistry, and engineering*. Boca Raton, FL: CRC Press.

Vickery, P. J., F. J. Masters, M. D. Powell, and D. Wadhera. 2009. "Hurricane hazard modeling: The past, present, and future." *J. Wind Eng. Ind. Aerodyn.* 97 (7): 392–405. https://doi.org/10.1016/j.jweia.2009.05.005.

Wang, H., T. Wu, T. Tao, A. Li, and A. Kareem. 2016. "Measurements and analysis of non-stationary wind characteristics at Sutong Bridge in Typhoon Damrey." *J. Wind Eng. Ind. Aerodyn.* 151 (Apr): 100–106. https://doi.org/10.1016/j.jweia.2016.02.001.

Wang, J., S. Cao, W. Pang, and J. Cao. 2017. "Experimental study on effects of ground roughness on flow characteristics of tornado-like vortices." *Bound.-Layer Meteorol.* 162 (2): 319–339. https://doi.org/10.1007/s10546-016-0201-6.

Wu, B., X. Chen, Q. Wang, H. Liao, and J. Dong. 2020. "Characterization of vibration amplitude of nonlinear bridge flutter from section model test to full bridge estimation." *J. Wind Eng. Ind. Aerodyn.* 197 (Feb): 104048. https://doi.org/10.1016/j.jweia.2019.104048.

Xia, J., K. Li, and Y. Ge. 2021. "Wind tunnel testing and frequency domain buffeting analysis of a 5000 m suspension bridge." *Adv. Struct. Eng.* 24 (7): 1326–1342. https://doi.org/10.1177/1369433220975568.

Xiang, H., and Y. Ge. 2002. "Refinements on aerodynamic stability analysis of super long-span bridges." *J. Wind Eng. Ind. Aerodyn.* 90 (12–15): 1493–1515. https://doi.org/10.1016/S0167-6105(02)00266-0.

Zhang, M., F. Xu, Z. Zhang, and X. Ying. 2019. "Energy budget analysis and engineering modeling of post-flutter limit cycle oscillation of a bridge deck." *J. Wind Eng. Ind. Aerodyn.* 188 (May): 410–420. https://doi.org/10.1016/j.jweia.2019.03.010.

Zhang, R., Z. Liu, L. Wang, and Z. Chen. 2021. "A practical method for predicting post-flutter behavior of a rectangular section." *J. Wind Eng. Ind. Aerodyn.* 216 (Sep): 104707. https://doi.org/10.1016/j.jweia.2021.104707.

Zhao, L., W. Cui, and Y. Ge. 2019. "Measurement, modeling and simulation of wind turbulence in typhoon outer region." *J. Wind Eng. Ind. Aerodyn.* 195 (Dec): 104021. https://doi.org/10.1016/j.jweia.2019.104021.

Zhao, L., T. Ma, W. Cui, and Y. Ge. 2023. "Finite element based study on aerostatic post-buckling and multi-stability of long-span bridges." *Struct. Infrastruct. Eng.* (Jan): 1–15. https://doi.org/10.1080/15732479.2022.2164596.